Temperature-Balancing Control for Modular Multilevel Converters Under Unbalanced Grid Voltages

Deng, Fujin; Zhao, Jifeng; Liu, Chengkai; Wang, Zheng; Cai, Xu; Blaabjerg, Frede

Published in:
I E E E Transactions on Power Electronics

DOI (link to publication from Publisher):
10.1109/TPEL.2021.3123634

Publication date:
2022

Document Version
Accepted author manuscript, peer reviewed version

Citation for published version (APA):
Deng, F., Zhao, J., Liu, C., Wang, Z., Cai, X., & Blaabjerg, F. (2022). Temperature-Balancing Control for Modular Multilevel Converters Under Unbalanced Grid Voltages. *I E E E Transactions on Power Electronics*, *37*(4), 4614-4625. Article 9594660. https://doi.org/10.1109/TPEL.2021.3123634

Temperature-Balancing Control for Modular Multilevel Converters under Unbalanced Grid Voltages

Fujin Deng, *Senior Member, IEEE*, Jifeng Zhao, Chengkai Liu, Zheng Wang, *Senior Member, IEEE*, Xu Cai and Frede Blaabjerg, *Fellow, IEEE*

***Abstract*- The modular multilevel converter (MMC) is attractive for medium-voltage and high-power applications because of the advantages of its high modularity, availability and high power quality. Due to unbalanced grid voltages, the arm current among three phases of the MMC would unbalance, which would cause unbalanced temperature distribution among three phases of MMCs and affect the reliability of MMCs. This paper proposes a variable frequency (VF) control strategy, which can effectively realize balanced temperature distribution among three phases of MMCs through adjusting carrier frequency in each phase to regulating device's switching loss in each phase of the MMC under unbalanced grid voltages. The proposed VF control can effectively improve the reliability of the MMC with the balanced temperature distribution among three phases of the MMC under unbalanced grid voltages. Simulation studies with the time-domain professional tool PSCAD/EMTDC and experimental studies with a down-scale MMC prototype are conducted to confirm the effectiveness of the proposed control.**

***Index Terms*- modular multilevel converter, temperature control, unbalanced grid voltages, variable frequency.**

I. INTRODUCTION

The Modular multilevel converter (MMC) was first proposed in the early 2000s [1]. It consists of a number of cascaded submodules (SMs) to produce multilevel voltage configuration [2-3]. Due to the features such as modularity and scalability, the MMC is attractive for medium-voltage and high-power application [4-5].

The grid voltages are normally allowed to be unbalanced temporarily in normal situation as indicated in the grid code [6], where the grid voltage is allowed to be between 0.9 p.u. and 1.1 p.u. and the possible maximum unbalanced degree of the grid voltage is allowed to reach 4% temporarily in normal situation. However, unbalanced grid voltages will result in unbalanced temperature distribution among three phases of MMCs and thus threatening the reliability of MMCs [7]-[8].

The temperature regulation is essential for the MMC to improve reliability. Recently, a number of methods have been reported to regulate the temperature for MMCs, which can be divided into SM design optimization-based method, SM capacitor voltage control-based method, and circulating current control-based method.

SM design optimization-based method can regulate the temperature of MMCs. Reference [9] presents a half-bridge SM with an additional antiparallel silicon-controlled thyristor, which can reduce the temperature stress of bottom diode in MMCs. References [10] and [11] introduce a SM topology with two-way bypass thyristor at the low side, which can regulate temperature stress of bottom IGBT/diode in the MMC. However, the above method complicates the hardware design.

SM capacitor voltage control-based method also plays an important role in temperature regulation of MMCs. Reference [12] presents a temperature optimization method by adjusting SM capacitor voltage to achieve an even thermal distribution among different SMs in the arm of MMCs. References [13-15] present a temperature optimization method which takes into account the capacitor voltage and the junction temperature of power device in each SM to balance the temperature among the power devices. However, the above method increases differences in capacitor voltage spread among the SMs.

Circulating current control-based methods have been proposed to regulate the temperature of the power device in the SM of MMCs. References [16] introduces a temperature optimization control method by controlling the second-order harmonic circulating current in the arm to limit the amplitude of junction temperature variation. Reference [17] proposes a second-order harmonic circulating current optimization control method by reducing the arm current peak value, which is able to reduce temperature stress of the power device in the SM. References [18] presents a temperature optimization control method, where the maximum temperature stress in the IGBT/diode of each SM can be effectively reduced through injecting optimum second-order harmonic current into the circulating current of MMCs. However, the above method needs injection of circulating current into the MMC, which increases power loss of MMCs.

In this paper, the temperature distribution of the MMC under unbalanced grid voltages is analyzed in details, where the unbalanced grid voltages would cause unbalanced arm currents distribution among three phases of the MMC. Thus, it would result in unbalanced temperature distribution among three phases of the MMC, and therefore affect the reliability of the three-phase MMC. In this paper, a variable frequency (VF) strategy is proposed for the MMC under unbalanced grid voltages, through adjusting the carrier frequency in each phase, the temperature of the power device among three phases can be effectively controlled to be balanced. The VF strategy can mitigate the thermal stress asymmetry among three phases of the MMC under unbalanced grid voltages, and therefore improves the reliability of the MMC.

The rest of this paper is organized as follows. Section II describes the MMC. Section III analyzes the thermal unbalance of MMCs under unbalanced grid voltages. Section IV proposes the VF strategy for MMCs. To verify the effectiveness of proposed strategy, Sections V and VI present the system simulation and experimental tests, respectively. Finally, the conclusions are presented in Section VII.

II. Descriptions of MMCs

A. Operation of MMCs

Fig. 1 shows a three-phase MMC tied to the grid. Each phase of the MMC has an upper arm and a lower arm. Each arm is composed of N identical SMs and an arm inductor L_s. Each SM contains two switches T_1, T_2 and a dc capacitor C. Each SM is controlled with a switching function as

$$S=\begin{cases}1, & T_1 \text{ is on and } T_2 \text{ is off} \\ 0, & T_1 \text{ is off and } T_2 \text{ is on}\end{cases} \tag{1}$$

When S=1, the T_1 is switched on and T_2 is switched off, and accordingly the SM is inserted into the arm. When S=0, the T_1 is switched off and T_2 is switched on, and accordingly the SM is bypassed from the arm [19].

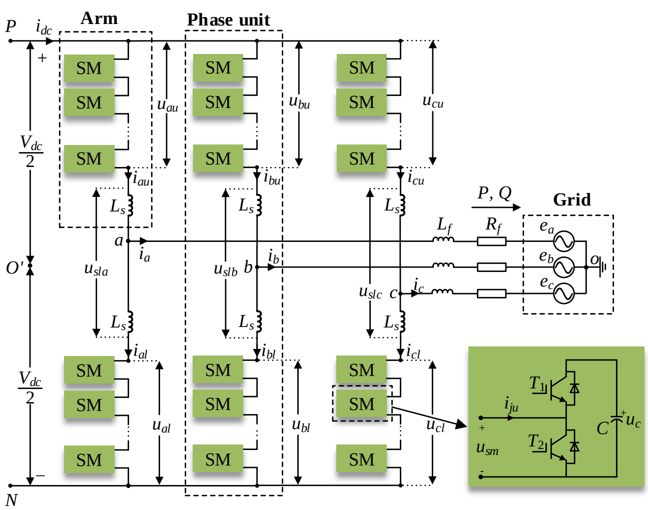

Fig. 1 A three-phase MMC.

B. SM Control

The SM individual voltage-balancing control is adopted for the MMC. Fig. 2 shows the control for the i-th SM in upper arm of phase A, which mainly consists of voltage averaging control (VAC) and voltage balancing control (VBC) [20]. The VAC is employed to force the average voltage $u_{c\_ave\_a}$ of the SMs in phase A to follow its command u_{c_ref}. The VBC is employed to force the i-th SM capacitor voltage u_{cau_i} to follow its command u_{c_ref}. With the VAC, VBC, the reference voltage u_{au_ref} for upper arm of phase A, and the dc-link voltage V_{dc}, the reference signal y_{au_i} for the i-th SM can be obtained. Through the comparison between the reference y_{au_i} and the carrier W_{ai} for the i-th SM, the switching function S_{au_i} for the i-th SM can be produced, where S_{au_i}=1 when y_{au_i} is more than W_{ai}; S_{au_i}=0 when y_{au_i} is less than W_{ai}. The W_{ai} is isosceles triangle between 0 and 1, whose frequency is f_w.

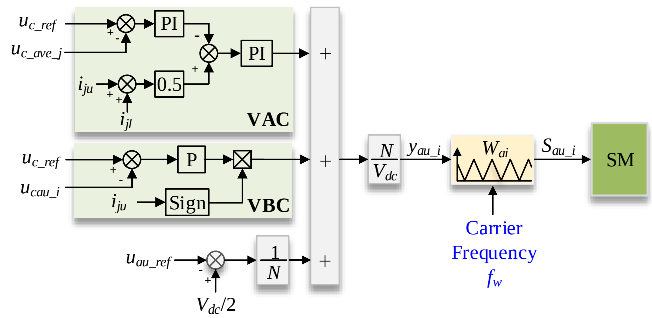

Fig. 2. Individual voltage-balancing control for the i-th SM in upper arm of phase A of the MMC.

III. Temperature Analysis of MMCs Under Unbalanced Grid Voltages

A. Unbalanced Grid Voltages

The unbalanced grid voltages e_a, e_b and e_c contain the positive-sequence and negative-sequence components, as

$$\begin{cases} e_a(t)=\sqrt{2}E_p\sin(\omega t)+\sqrt{2}E_n\sin(\omega t+\theta) \\ e_b(t)=\sqrt{2}E_p\sin(\omega t-\dfrac{2\pi}{3})+\sqrt{2}E_n\sin(\omega t+\theta+\dfrac{2\pi}{3}) \\ e_c(t)=\sqrt{2}E_p\sin(\omega t+\dfrac{2\pi}{3})+\sqrt{2}E_n\sin(\omega t+\theta-\dfrac{2\pi}{3}) \end{cases} \tag{2}$$

where E_p and E_n are the root mean square values of the positive-sequence voltage and negative-sequence voltage, respectively. θ is phase angle. ω is the fundamental angular frequency. According to the grid code [6], the unbalanced degree of the grid voltage is

$$\varepsilon=\frac{E_n}{E_p}\times 100\% \tag{3}$$

In the grid code [6], the grid voltage magnitude is allowed to be between 0.9 p.u. and 1.1 p.u. and the possible maximum unbalanced degree of the grid voltage is allowed to reach 4% temporarily in the normal operation situation. According to grid code [6] and (2), Fig. 3 shows the operation area of the grid voltage under the normal operation situation, where each grid voltage corresponds to an (E_p, E_n, θ), as shown in (2).

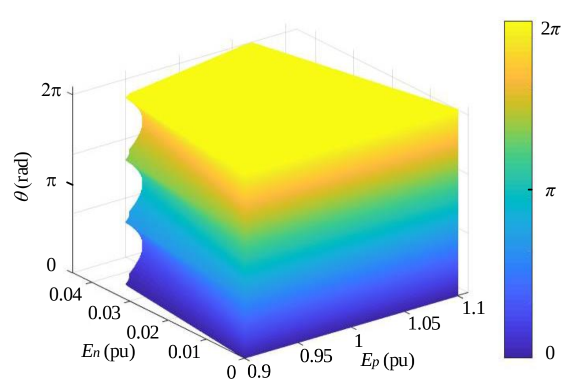

Fig. 3 Operation area of the grid voltage.

B. Analysis of Grid Currents

In Fig. 1, the dynamics of the MMC can be expressed as

$$\begin{cases} u_{ea}(t)=(u_{al}\text{-}u_{au})/2=L\dfrac{di_a(t)}{dt}+R_f i_a(t)+e_a(t) \\ u_{eb}(t)=(u_{bl}\text{-}u_{bu})/2=L\dfrac{di_b(t)}{dt}+R_f i_b(t)+e_b(t) \\ u_{ec}(t)=(u_{cl}\text{-}u_{cu})/2=L\dfrac{di_c(t)}{dt}+R_f i_c(t)+e_c(t) \end{cases} \tag{4}$$

where u_{ea}, u_{eb}, u_{ec} are the ac electromotive forces (EMFs) of the MMC. u_{ju} and u_{jl} are the total SM output voltage in the upper and lower arm of phase j (j=a, b, c), respectively. L=L_s/2+L_f. L_f and R_f are filter inductor and resistor, respectively.

According to (4) and [21], the dynamics of the MMC in the positive and negative rotating references can be expressed as

$$\frac{d}{dt}\begin{bmatrix} i_d^p \\ i_q^p \end{bmatrix}=\begin{bmatrix} -\dfrac{R_f}{L} & \omega \\ -\omega & -\dfrac{R_f}{L} \end{bmatrix}\cdot\begin{bmatrix} i_d^p \\ i_q^p \end{bmatrix}-\frac{1}{L}\begin{bmatrix} e_d^p \\ e_q^p \end{bmatrix}+\frac{1}{L}\begin{bmatrix} u_d^p \\ u_q^p \end{bmatrix} \tag{5}$$

$$\frac{d}{dt}\begin{bmatrix} i_d^n \\ i_q^n \end{bmatrix}=\begin{bmatrix} -\dfrac{R_f}{L} & -\omega \\ \omega & -\dfrac{R_f}{L} \end{bmatrix}\cdot\begin{bmatrix} i_d^n \\ i_q^n \end{bmatrix}-\frac{1}{L}\begin{bmatrix} e_d^n \\ e_q^n \end{bmatrix}+\frac{1}{L}\begin{bmatrix} u_d^n \\ u_q^n \end{bmatrix} \tag{6}$$

where i_d^p and i_q^p are the positive-sequence components of the grid current in the dq reference frame. i_d^n and i_q^n are the negative-sequence components of the grid current in the dq reference frame. e_d^p and e_q^p are the positive-sequence components of the grid voltage in the dq reference frame. The e_d^n and e_q^n are the negative-sequence components of the grid voltage in the dq reference frame. The u_d^p and u_q^p are the positive-sequence MMC voltage in the dq reference frame. u_d^n and u_q^n are the negative-sequence MMC voltage in the dq reference frame.

The active power P and reactive power Q in grid are [21]

$$\begin{cases} P=P_0+P_{s2}\sin(2\omega t)+P_{c2}\cos(2\omega t) \\ Q=Q_0+Q_{s2}\sin(2\omega t)+Q_{c2}\cos(2\omega t) \end{cases} \tag{7}$$

with

$$\begin{bmatrix} P_0 \\ Q_0 \\ P_{s2} \\ P_{c2} \\ Q_{s2} \\ Q_{c2} \end{bmatrix}=\frac{3}{2}\begin{bmatrix} e_d^p & e_q^p & e_d^n & e_q^n \\ e_q^p & -e_d^p & e_q^n & -e_d^n \\ e_q^n & -e_d^n & -e_q^p & e_d^p \\ e_d^n & e_q^n & e_d^p & e_q^p \\ -e_d^n & -e_q^n & e_d^p & e_q^p \\ e_q^n & -e_d^n & e_q^p & -e_d^p \end{bmatrix}\begin{bmatrix} i_d^p \\ i_q^p \\ i_d^n \\ i_q^n \end{bmatrix} \tag{8}$$

where P_0 and Q_0 are the average value of the instantaneous active and reactive power. P_{s2}, P_{c2} and Q_{s2}, Q_{c2} are the sine and cosine peak value of the active and reactive power, respectively.

According to (4)~(6), the vector control [21] including positive-sequence and negative-sequence control is adopted for the MMC, where the positive-sequence voltage is aligned to the d-axis of the positive rotating reference and the negative-sequence control is used to eliminate the negative-sequence current. As a result, the positive-sequence voltage and the negative-sequence current are

$$\begin{cases} e_d^p=\sqrt{2}E_p \\ e_q^p=0 \\ i_d^n=0 \\ i_q^n=0 \end{cases} \tag{9}$$

According to (7)~(9), the grid current can be obtained as

$$\begin{cases} i_a(t)=I_m\sin(\omega t+\varphi) \\ i_b(t)=I_m\sin(\omega t+\varphi-\dfrac{2\pi}{3}) \\ i_c(t)=I_m\sin(\omega t+\varphi+\dfrac{2\pi}{3}) \end{cases} \tag{10}$$

with

$$\begin{cases} I_m=\dfrac{\sqrt{2}}{3}\dfrac{\sqrt{P_0^2+Q_0^2}}{E_p} \\ \varphi=\arctan\dfrac{i_q^p}{i_d^p}=\arctan(\dfrac{-Q_0}{P_0}) \end{cases} \tag{11}$$

C. Analysis of Arm Currents

According to (2) and (10), the average power in the phase A, B and C can be expressed as

$$\begin{cases} P_a=\dfrac{1}{T}\int_0^T e_a(t)\cdot i_a(t)dt \\ P_b=\dfrac{1}{T}\int_0^T e_b(t)\cdot i_b(t)dt \\ P_c=\dfrac{1}{T}\int_0^T e_c(t)\cdot i_c(t)dt \end{cases} \tag{12}$$

where T is the fundamental cycle and T=2π/ω.

Neglecting the power losses in the filter resistor R_f, the power will be balanced between the ac side and the dc side in each phase of the MMC as

$$\begin{cases} P_a=i_{dca}\cdot V_{dc} \\ P_b=i_{dcb}\cdot V_{dc} \\ P_c=i_{dcc}\cdot V_{dc} \end{cases} \tag{13}$$

where i_{dca}, i_{dcb}, i_{dcc} are the dc components in the arm currents of phase A, B and C, respectively. Substituting (2), (10) and (11) into (13), the dc components i_{dca}, i_{dcb}, i_{dcc} in the arm currents of phase A, B and C can be obtained as

$$\begin{cases} i_{dca}=\dfrac{P_0}{3V_{dc}}+\Delta i_{dca} \\ i_{dcb}=\dfrac{P_0}{3V_{dc}}+\Delta i_{dcb} \\ i_{dcc}=\dfrac{P_0}{3V_{dc}}+\Delta i_{dcc} \end{cases} \tag{14}$$

with

$$\begin{cases} \Delta i_{dca} = \varepsilon \dfrac{\sqrt{P_0^2 + Q_0^2}}{3V_{dc}} \sin(\theta + \varphi) \\ \Delta i_{dcb} = \varepsilon \dfrac{\sqrt{P_0^2 + Q_0^2}}{3V_{dc}} \sin(\theta - \dfrac{2\pi}{3} + \varphi) \\ \Delta i_{dcc} = \varepsilon \dfrac{\sqrt{P_0^2 + Q_0^2}}{3V_{dc}} \sin(\theta + \dfrac{2\pi}{3} + \varphi) \end{cases} \tag{15}$$

where Δi_{dca}, Δi_{dcb}, Δi_{dcc} are the deviations in phase A, B and C, respectively. In addition, $\Delta i_{dca}+\Delta i_{dcb}+\Delta i_{dcc}=0$.

According to (14) and (15), the unbalanced grid voltages cause Δi_{dca}, Δi_{dcb}, Δi_{dcc} in phase A, B and C, and therefore cause different i_{dca}, i_{dcb}, i_{dcc}. Along with the increase of the unbalanced degree ε, the deviation would be increased, where the $Max[\Delta i_{dca}, \Delta i_{dcb}, \Delta i_{dcc}]$ would be increased and the $Min[\Delta i_{dca}, \Delta i_{dcb}, \Delta i_{dcc}]$ would be reduced, and therefore the $Max[i_{dca}, i_{dcb}, i_{dcc}]$ would be increased and the $Min[i_{dca}, i_{dcb}, i_{dcc}]$ would be reduced, and vice versa, as shown in Table I. Here, the maximum deviations of $Max[i_{dca}, i_{dcb}, i_{dcc}]$ and $Min[i_{dca}, i_{dcb}, i_{dcc}]$ appear when ε reaches its maximum.

TABLE I
RELATIONSHIP BETWEEN ε AND DEVIATION

ε	$Max[\Delta i_{dca}, \Delta i_{dcb}, \Delta i_{dcc}]$	$Min[\Delta i_{dca}, \Delta i_{dcb}, \Delta i_{dcc}]$	$Max[i_{dca}, i_{dcb}, i_{dcc}]$	$Min[i_{dca}, i_{dcb}, i_{dcc}]$
↑	↑	↓	↑	↓
↓	↓	↑	↓	↑

Suppose that the second-order circulating current is eliminated by the circulating current suppression control [22], the arm current is only composed of the dc component and the fundamental component in the MMC. According to (10) and (14), the arm current in the MMC can be obtained as

$$\begin{cases} i_{au,al}(t) = \pm\dfrac{i_a}{2} + i_{dca} \\ \quad = \underbrace{\pm\dfrac{\sqrt{2}}{6}\dfrac{\sqrt{P_0^2+Q_0^2}}{E_p}\sin(\omega t+\varphi)}_{\text{AC fundamental component}} + \underbrace{\dfrac{P_0}{3V_{dc}} + \Delta i_{dca}}_{\text{DC component}} \\ i_{bu,bl}(t) = \pm\dfrac{i_b}{2} + i_{dcb} \\ \quad = \underbrace{\pm\dfrac{\sqrt{2}}{6}\dfrac{\sqrt{P_0^2+Q_0^2}}{E_p}\sin(\omega t+\varphi-\dfrac{2\pi}{3})}_{\text{AC fundamental component}} + \underbrace{\dfrac{P_0}{3V_{dc}} + \Delta i_{dcb}}_{\text{DC component}} \\ i_{cu,cl}(t) = \pm\dfrac{i_c}{2} + i_{dcc} \\ \quad = \underbrace{\pm\dfrac{\sqrt{2}}{6}\dfrac{\sqrt{P_0^2+Q_0^2}}{E_p}\sin(\omega t+\varphi+\dfrac{2\pi}{3})}_{\text{AC fundamental component}} + \underbrace{\dfrac{P_0}{3V_{dc}} + \Delta i_{dcc}}_{\text{DC component}} \end{cases} \tag{16}$$

From (16), it can be observed that the AC component in the arm currents of different phases are symmetrical, while the DC components in the arm currents of different phases are different under the unbalanced grid voltages.

D. Analysis of Device Power Losses

The power loss of a power device contain the conduction loss and switching loss. The average conduction loss P_{con_ave} of a power device is [23]

$$P_{con\_ave} = \frac{1}{T}\int_0^T p_{con\_inst}(t)dt \tag{17}$$

with

$$p_{con\_inst}(t) = [u_{ceo} + r_c \cdot i_x(t)] \cdot i_x(t) \tag{18}$$

where p_{con_inst} is instantaneous conduction loss. u_{ceo} and r_c are switch on-state zero-current collector-emitter voltage and collector-emitter on-state resistance, respectively. i_x is the conducting current through the power device.

The average switching loss P_{sw_ave} of a power device is [23]

$$P_{sw\_ave} = \frac{1}{T}\int_0^T e_{sw\_inst}(t)dt \tag{19}$$

with

$$e_{sw\_inst}(t) = f_w \cdot E_{sw}(i_x(t)) \cdot \frac{U_{sm}}{U_{ref}} \tag{20}$$

where e_{sw_inst} is instantaneous switching energy loss. E_{sw} is the switching energy loss, which increases along with the increase of i_x and reduces along with the reduction of i_x. U_{sm} is the average capacitor voltage of the SM. U_{ref} is the reference blocking voltage in the data sheet.

The average power loss P_{ave} of a power device is

$$P_{ave} = P_{con\_ave} + P_{sw\_ave} \tag{21}$$

According to (17)~(21), it can be observed that the P_{ave} increases along with the increase of i_x; P_{ave} reduces along with the reduction of i_x. The unbalanced grid voltages result in different dc component in the arm current, and therefore cause different power losses for the same power device in the three phases. The $P_{con\_ave\_j}$, $P_{sw\_ave\_j}$ and P_{ave_j} of the power device increases along with the increase of the dc component i_{dcj} in the arm current and the $P_{con\_ave\_j}$, $P_{sw\_ave\_j}$ and P_{ave_j} of the power device reduces along with the reduction of the i_{dcj} in the arm current, as shown in Table II.

TABLE II
RELATIONSHIP BETWEEN $P_{con\_ave\_j}$, $P_{sw\_ave\_j}$, P_{ave_j} AND i_{dcj}

i_{dcj}	$P_{con\_ave\_j}$	$P_{sw\_ave\_j}$	P_{ave_j}
↑	↑	↑	↑
↓	↓	↓	↓

According to Tables I and II, along with the increase of ε, the $Max[P_{ave\_a}, P_{ave\_b}, P_{ave\_c}]$ would be increased and the $Min[P_{ave\_a}, P_{ave\_b}, P_{ave\_c}]$ would be reduced. Consequently, the maximum power losses difference ($Max[P_{ave\_a}, P_{ave\_b}, P_{ave\_c}]$-$Min[P_{ave\_a}, P_{ave\_b}, P_{ave\_c}]$) among three phases appears when ε reaches its maximum value, as shown in Table III.

TABLE III
RELATIONSHIP BETWEEN ε AND POWER LOSS DIFFERENCE

ε	$Max[P_{ave\_a}, P_{ave\_b}, P_{ave\_c}]$	$Min[P_{ave\_a}, P_{ave\_b}, P_{ave\_c}]$	Max. loss difference
↑	↑	↓	↑
↓	↓	↑	↓

E. Analysis of Device Temperature

The equivalent thermal network diagram of a device is shown in Fig. 4, which consists of the thermal resistance $R_{th(J-C)}$ of the device from junction to case and the thermal resistance $R_{th(C-H)}$ of thermal interface material (TIM) from case to heat sink [24-25]. Based on this model, the average junction temperature T_{ave} of a device can be expressed as

$$T_{ave} = (R_{th(J-C)} + R_{th(C-H)}) \cdot P_{ave} + T_H \tag{22}$$

where T_H is the temperature of heat sink. To simplify the analysis, the T_H is considered as a constant value 50°C.

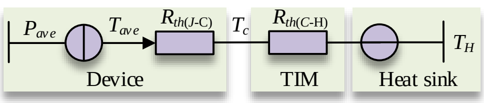

Fig. 4. Thermal network of a device.

According to (22), different power losses P_{ave_a}, P_{ave_b}, P_{ave_c} in three phases derived from the unbalanced grid voltages would cause different temperatures T_{ave_a}, T_{ave_b}, T_{ave_c} for the same power device in three phases. The T_{ave} of the power device increases along with the increase of the P_{ave}, and vice versa, as shown in Table IV.

TABLE IV
RELATIONSHIP BETWEEN T_{ave_j} AND P_{ave_j}

P_{ave_j}	T_{ave_j}
↑	↑
↓	↓

According to Tables III and IV, along with the increase of ε, the $Max[T_{ave\_a}, T_{ave\_b}, T_{ave\_c}]$ is increased and the $Min[T_{ave\_a}, T_{ave\_b}, T_{ave\_c}]$ is reduced. Consequently, the maximum temperature difference ($Max[T_{ave\_a}, T_{ave\_b}, T_{ave\_c}]$-$Min[T_{ave\_a}, T_{ave\_b}, T_{ave\_c}]$) among the three phases of the MMC appears when ε reaches its maximum value, as shown in Table V.

TABLE V
RELATIONSHIP BETWEEN ε AND TEMPERATURE DEVIATION

ε	$Max[T_{ave\_a}, T_{ave\_b}, T_{ave\_c}]$	$Min[T_{ave\_a}, T_{ave\_b}, T_{ave\_c}]$	Max. temperature difference
↑	↑	↓	↑
↓	↓	↑	↓

In Fig. 1, the T_2 takes the maximum power loss and the maximum temperature among the power devices in the SM when the MMC works in inverter mode [26-27]. Fig. 5 shows the T_2's power loss in phases A, B, C and the maximum power loss difference of T_2 among phases A, B, C. Fig. 5 also shows the T_2's temperature in phases A, B, C and the maximum temperature difference of T_2 among phases A, B, C. Here, the ε reaches the maximum. It can be observed that the power loss (temperature) of T_2 in phase A, B, C and the maximum power loss (temperature) difference of T_2 varies along with the change of (E_p, θ).

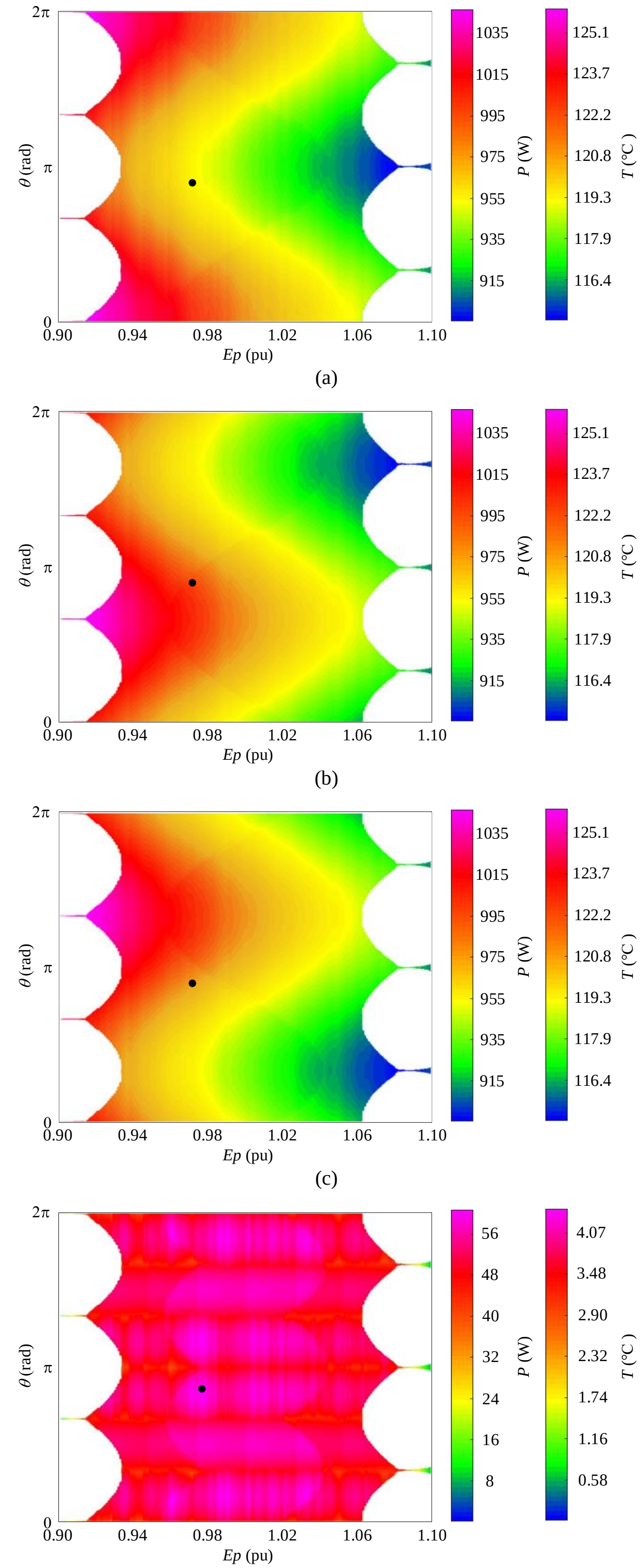

Fig. 5. Power loss and temperature of T_2 under maximum ε. (a) Power loss and temperature in phase A. (b) Power loss and temperature in phase B. (c) Power loss and temperature in phase C. (d) Maximum power loss difference and maximum temperature difference among three phases.

IV. PROPOSED VF STRATEGY FOR MMCS

A. Proposed VF Approach

The power device's power loss P_{ave} contains the conduction loss P_{con_ave} and the switching loss P_{sw_ave}. The switching loss P_{sw_ave} is related to switching frequency f_w, as shown in (18), where the P_{sw_ave} is increased along with the increase of f_w, and the P_{sw_ave} is reduced along with the reduction of f_w. Based on above analysis, a VF approach is proposed, where the power device's P_{ave} and T_{ave} in the MMC can be regulated by f_w, as shown in Table VI, as follows.

1) Increase of f_w: the switching loss P_{sw_ave} is increased, while the conduction loss P_{con_ave} is nearly not affected. Consequently, the power loss P_{ave} is increased, which causes the increase of the junction temperature T_{ave} of the power device.
2) Decrease of f_w: the switching loss P_{sw_ave} is reduced, while the conduction loss P_{con_ave} is nearly not affected. Consequently, the power loss P_{ave} is reduced, which causes the reduction of the junction temperature T_{ave} of the power device.

TABLE VI
RELATIONSHIP BETWEEN f_{sw} AND P_{ave}, T_{em_ave}

f_w	P_{con_ave}	P_{sw_ave}	P_{ave}	T_{ave}
↑	—	↑	↑	↑
↓	—	↓	↓	↓

B. Proposed VF Strategy for MMCs under Unbalanced Grid Voltages

Based on above VF approach, a VF strategy is proposed to balance the temperature distribution of the power devices among three phases, as shown in Fig. 6.

Fig. 6(a) shows the positive-sequence and negative-sequence control of the MMC. According to the control objective such as active power and reactive power, the reference currents $i^p_{d\_ref}$ and $i^p_{q\_ref}$ in the positive-sequence reference can be obtained. With the vector control in the positive-sequence reference frame, the reference voltages $u^p_{abc\_ref}$ can be obtained to control the i^p_d and i^p_q to follow the reference currents $i^p_{d\_ref}$ and $i^p_{q\_ref}$, so as to realize the active power control and reactive power control. In addition, with the vector control in the negative-sequence reference frame, the reference voltages $u^n_{abc\_ref}$ are obtained to control the i^n_d and i^n_q to zero to eliminate the negative-sequence components of the grid current. Afterwards, the reference for the three phases of the MMC can be obtained as $y_{abc\_ref}=2(u^p_{abc\_ref}+u^n_{abc\_ref})/V_{dc}$.

Fig. 6(b) shows the detailed VF strategy for the three phases of MMCs. According to the device's temperatures T_{ave_a}, T_{ave_b}, and T_{ave_c} in phase A, B, and C of MMCs, respectively, the reference temperature T_{ave_ref} of the MMC can be obtained as $T_{ave\_ref}=(T_{ave\_a}+T_{ave\_b}+T_{ave\_c})/3$. For the three phases of the MMC, the PI controllers are used to regulate their carrier frequency f_{w_a}, f_{w_b}, and f_{w_c} to realize there-phase temperature balancing based on VF approach, as shown in Table VI. The rated carrier frequency f_r for each phase is 1000 Hz. The PI controller is used to produce the carrier frequency's compensation components f_a, f_b, and f_c in phase A, B and C, respectively. If the T_{ave_j} in phase j is less than the average temperature T_{ave_ref}, the PI controller would increase the f_j. As a result, the carrier frequency $f_{w\_j}=f_r+f_j$ in phase j is increased, and the T_{ave_j} is increased to follow T_{ave_ref}. If the T_{ave_j} in phase j is more than the T_{ave_ref}, the PI controller would reduce the f_j. As a result, the carrier frequency $f_{w\_j}=f_r+f_j$ in phase j is reduced, and the T_{ave_j} is reduced to follow T_{ave_ref}. As a result, the proposed VF strategy can effectively realize temperature balancing of the devices in the three phases of the MMC under unbalanced grid voltages.

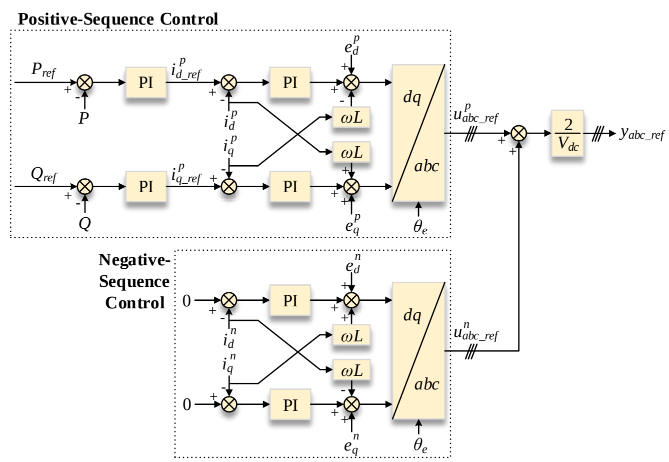

(a)

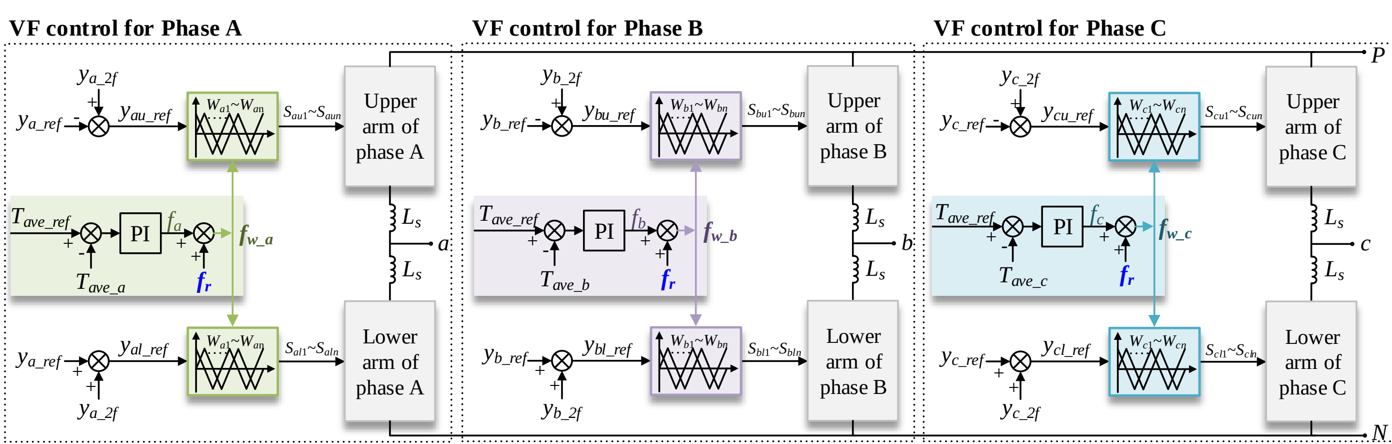

(b)

Fig. 6. Proposed VF strategy for MMCs under unbalanced grid voltages. (a) Positive-sequence and negative-sequence control of the MMC. (b) VF control for phase A, B and C.

C. Discussion of Proposed VF Strategy

Fig. 7 shows one example of the worst situations for the MMC under ε=4%, as the black point in Fig. 5, where the temperature in phase B is the maximum and the temperature in phase A is the minimum. The MMC system parameters are shown in Table VII. Figs. 7(a)~(d) show the conduction loss P_{con_ave}, switching loss P_{sw_ave}, average loss P_{ave} and temperature T_{ave} in phase A, B and C, respectively, under various carrier frequencies f_w. The conduction loss is nearly not affected by f_w. The switching loss, average loss and temperature increase along with the increase of f_w, and vice versa. At the rated frequency 1000 Hz, the power losses in three phases are unbalanced as P_{ave_a}=0.954 kW, P_{ave_b}=1.010 kW, and P_{ave_c}=0.987 kW; the temperature in three phases are unbalanced as T_{ave_a}=119.3 ºC, T_{ave_b}=123.3 ºC, and T_{ave_c}=121.7 ºC. With the proposed control, the power losses and temperature in three phases can be balanced as 0.984 kW and 121.4 ºC, respectively, through regulating their carrier frequencies. Figs. 7(c) and (d) show that the maximum change of the carrier frequency is only 96 Hz.

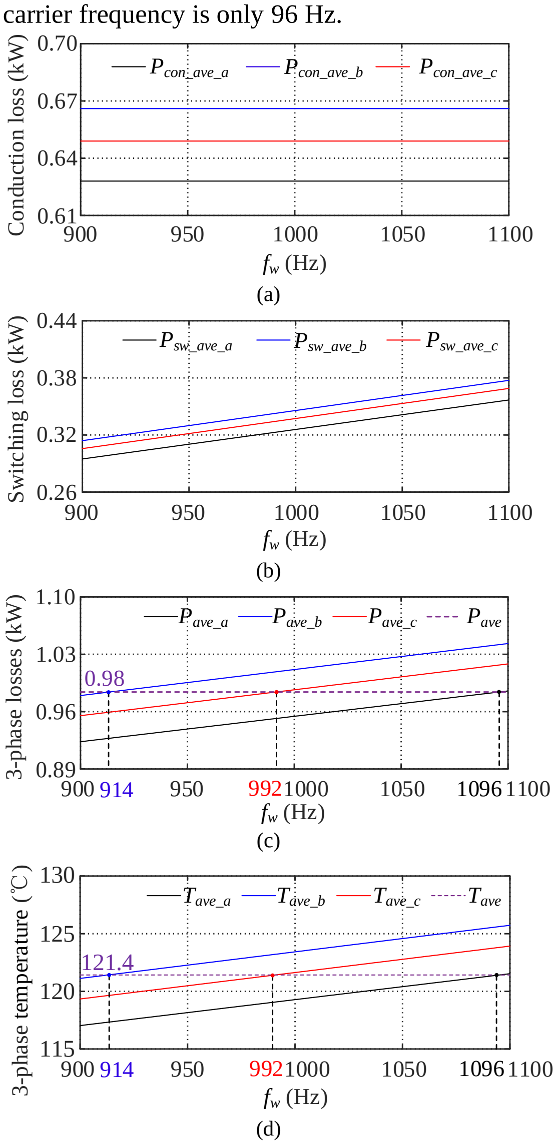

Fig. 7. MMC performance under various carrier frequencies. (a) Conduction loss. (b) Switching loss. (c) Average loss. (d) Average temperature.

V. Simulation Studies

To verify the proposed control, a three-phase MMC is built with the PSCAD/EMTDC, as shown in Fig. 8. The system parameters are shown in Table VII.

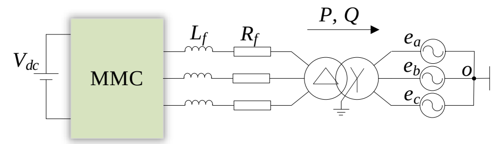

Fig. 8 Schematic diagram of simulation system.

TABLE VII
Simulation System Parameters

Parameters	Value
Active power (MW)	4.5
DC-link voltage V_{dc} (kV)	6
Grid line-to-line voltage (kV)	33
Grid frequency (Hz)	50
Transformer rating voltage	3 kV/33 kV
Number of SMs per arm n	6
Nominal SM capacitance C (mF)	15
Inductance L_s (mH)	2
Inductance L_f (mH)	1

A. Case I: Balanced Grid Voltages

Fig. 9 shows the performance of the three-phase MMC under balanced grid voltages, where the active power P is 4.5 MW. Figs. 9(a) and (b) show the grid voltages e_a, e_b, e_c and grid currents i_a, i_b, i_c. Fig. 9(c) shows the upper arm currents i_{ua}, i_{ub}, i_{uc} in phase A, phase B and phase C, respectively. Fig. 9 (d) shows that the T_2's power losses P_{ave_a}, P_{ave_b}, P_{ave_c} in phase A, phase B and phase C, respectively, are almost the same. Fig. 9(e) shows T_2's average junction temperatures T_{ave_a}, T_{ave_b}, T_{ave_c} in phase A, phase B and phase C, respectively, are almost the same.

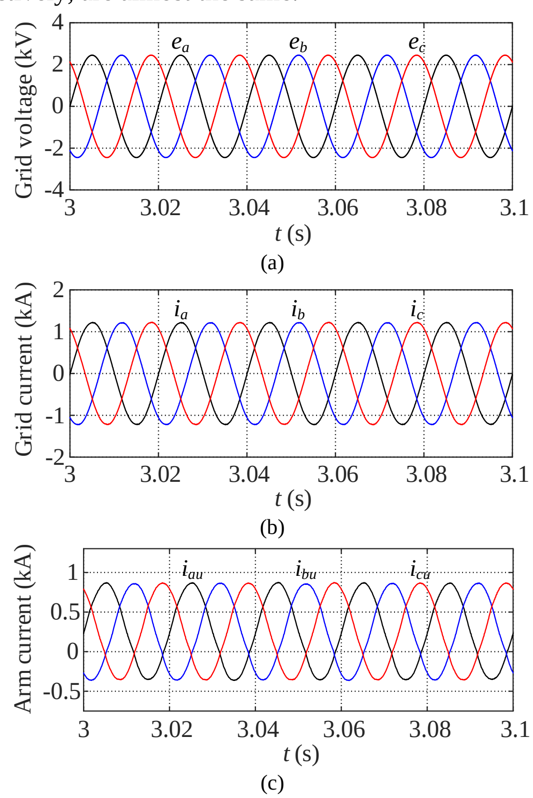

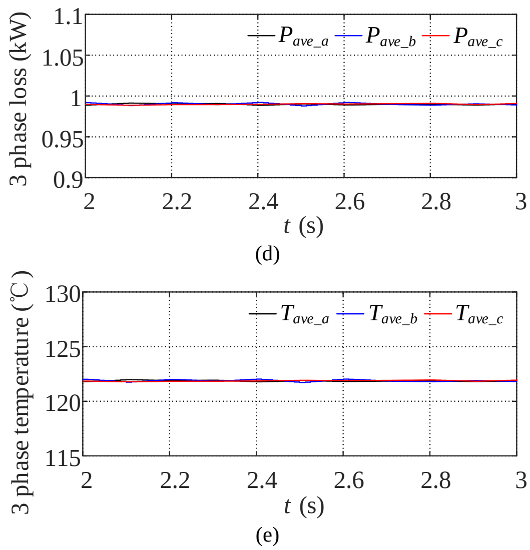

Fig. 9. (a) e_a, e_b and e_c. (b) i_a, i_b and i_c. (c) i_{au}, i_{bu} and i_{cu}. (d) P_{ave_a}, P_{ave_b} and P_{ave_c}. (e) T_{ave_a}, T_{ave_b} and T_{ave_c}.

B. Case II: Unbalanced Grid Voltages

Fig. 10 shows the performance of the three-phase MMC under unbalanced grid voltages, where the active power P is 4.5 MW, the grid voltage unbalanced degree is 4%. Here, the proposed strategy is enabled since 3.1s. Figs. 10(a) and (b) show the grid voltages e_a, e_b, e_c and grid currents i_a, i_b, i_c. Fig. 10(c) shows the upper arm currents i_{au}, i_{bu}, i_{cu} in three phases. Fig. 10(d) shows the carrier frequency f_{w_a}, f_{w_b}, f_{w_c} in three phases. Fig. 10 (e) shows that the T_2's power losses P_{ave_a}, P_{ave_b}, P_{ave_c} in three phases are unbalanced before 3.1s, where the maximum difference is about 0.06 kW. Fig. 10(f) shows the T_2's average junction temperature T_{ave_a}, T_{ave_b}, T_{ave_c} in three phases are unbalanced before 3.1s, where the maximum difference is about 4.2 °C. Since 3.1s, the proposed control is enabled, where the f_{w_a}, f_{w_b}, f_{w_c} are changed and stable at 1096 Hz, 914 Hz, 992 Hz, respectively. Here, the T_2's P_{ave_a}, P_{ave_b}, P_{ave_c} in phase A, phase B and phase C become balance and the T_2's T_{ave_a}, T_{ave_b}, T_{ave_c} in phase A, phase B and phase C becomes balance.

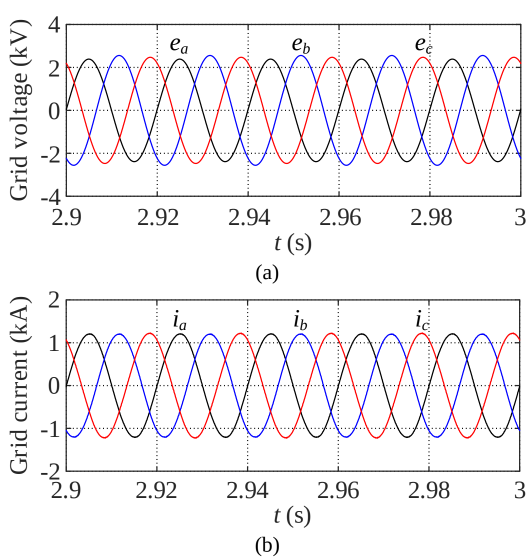

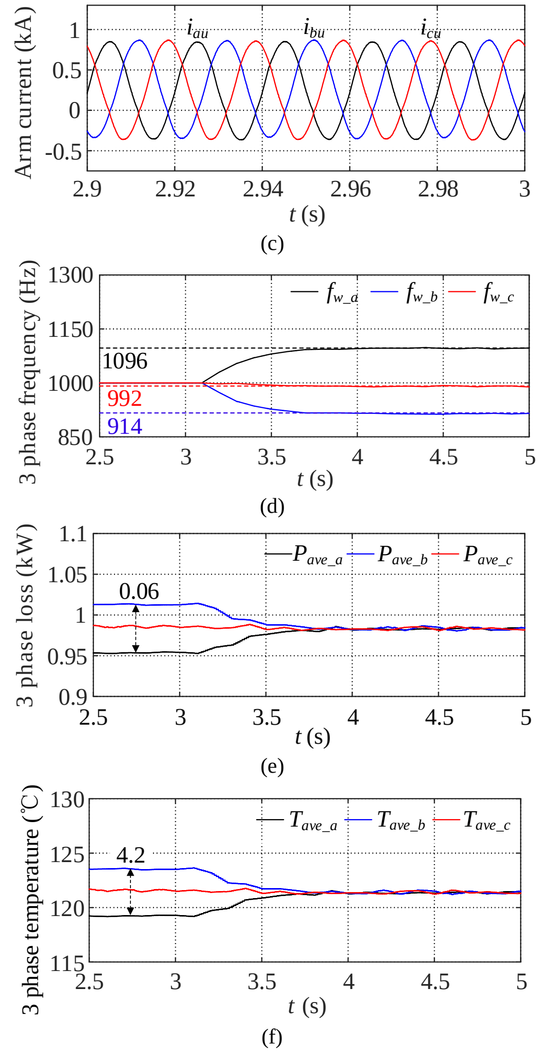

Fig. 10. (a) e_a, e_b and e_c. (b) i_a, i_b and i_c. (c) i_{au}, i_{bu} and i_{cu}. (d) f_{w_a}, f_{w_b} and f_{w_c}. (e) P_{ave_a}, P_{ave_b} and P_{ave_c}. (f) T_{ave_a}, T_{ave_b} and T_{ave_c}.

VI. EXPERIMENTAL STUDIES

A three-phase MMC set up is built in the laboratory to verify the proposed strategy, as shown in Figs. 11(a) and (b). The DC link of the MMC consist of a DC power supply (LAB/SMS6600) and the grid side of the MMC adopt grid emulator (Chroma AC source 61845). The digital signal process (DSP) controller executes system control algorithm and transfer drive signals through optical fibre to the gate driver of each SM. The FZ122PB100SC03 is used as the IGBT/diode, in which there is an inner thermistor R_t for measuring the heat sink temperature. A measuring circuit, as shown in Fig. 11(c), is designed in the SM board to measure R_t. In Fig. 11(c), the voltage V_1 can be directly measured and obtained, and therefore the R_t can be calculated as $(2.5-V_1)\cdot R_1/V_1$. And then, according to thermistor temperature characteristic $T_H=f(R_t)$ in IGBT module's datasheet, the heat sink temperature T_H can be obtained. Afterwards, according to the thermal model in Fig. 4 and (22), the junction temperature of the IGBT can be estimated. The detailed experimental platform parameters are shown in Table VIII.

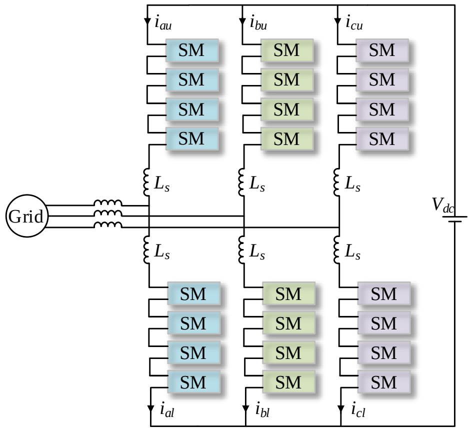

(a)

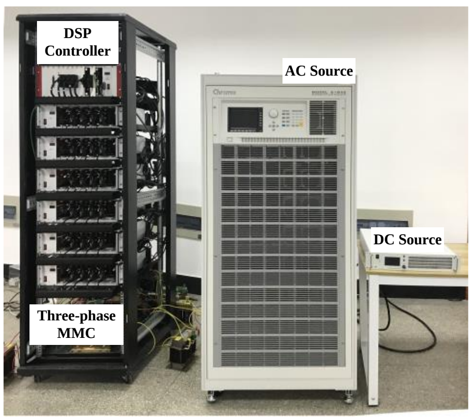

(b)

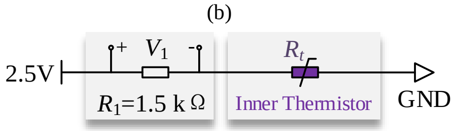

(c)

Fig. 11. Experimental system. (a) Block diagram of the experimental circuit. (b) Photo of experimental platform. (c) The heat sink temperature measuring circuit.

TABLE VIII
EXPERIMENTAL SYSTEM PARAMETERS

Parameter	Value
Rated Power (kW)	2
DC-link voltage V_{dc} (V)	300
RMS value of line-to-line (V)	123
Rated frequency (Hz)	50
Number of SM per arm N	4
SM capacitance (mF)	2.7
Arm inductance L_s (mH)	3
Carrier frequency (kHz)	5

A. Case I: Balanced Grid Voltages

Fig. 12 shows the performance of the three-phase MMC under balanced grid voltages. Fig. 12(a) shows the three-phase grid voltages e_a, e_b, e_c. Fig. 12(b) shows the three-phase grid currents i_a, i_b, i_c. Fig. 12(c) shows the upper arm currents i_{au}, i_{bu}, i_{cu} in phase A, phase B and phase C. Fig. 12 (d) shows that the T_2's power loss P_{ave_a}, P_{ave_b}, P_{ave_c} in phase A, phase B and phase C are almost the same. Fig. 12(e) shows that the T_2's average junction temperature T_{ave_a}, T_{ave_b}, T_{ave_c} in phase A, phase B and phase C are almost the same.

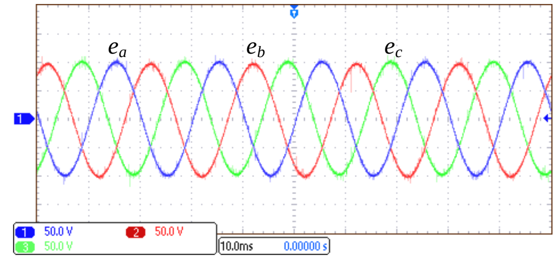

(a)

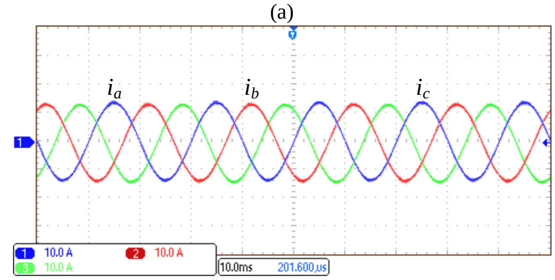

(b)

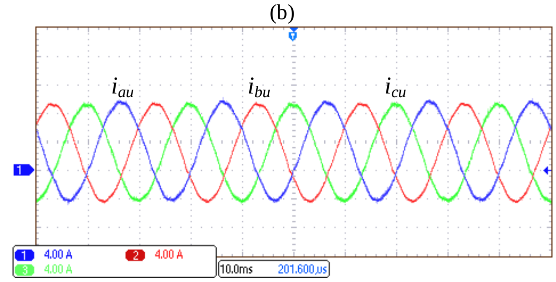

(c)

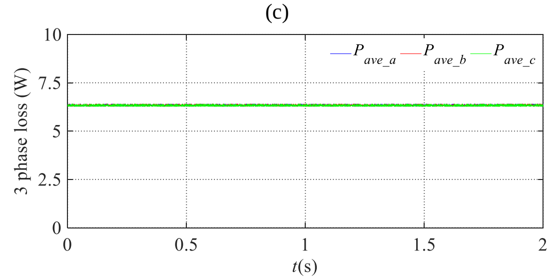

(d)

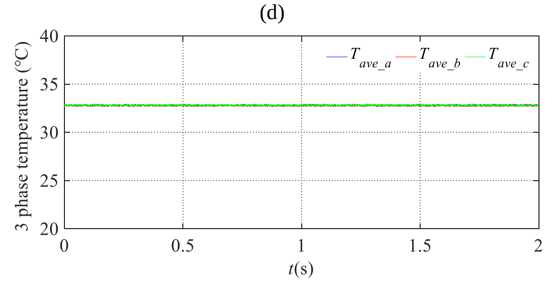

(e)

Fig. 12. (a) e_a, e_b and e_c. (b) i_a, i_b, and i_c. (c) i_{au}, i_{bu} and i_{cu}. (d) P_{ave_a}, P_{ave_b} and P_{ave_c}. (e) T_{ave_a}, T_{ave_b} and T_{ave_c}.

B. Case II: Unbalanced Grid Voltages

Fig. 13 shows the performance of the three-phase MMC under unbalanced grid voltages, where the active power P is 2 kW. Here, the grid voltage unbalanced degree is 14% and the proposed control is enabled since 30.74s. Figs. 13(a) and (b) show the grid voltages e_a, e_b, e_c and grid currents i_a, i_b, i_c. Fig. 13(c) shows the upper arm currents i_{au}, i_{bu}, i_{cu} in phase A, phase B and phase C, respectively. Fig. 13 (d) shows that the T_2's power losses P_{ave_a}, P_{ave_b}, P_{ave_c} in phase A, phase B and phase C are unbalanced before 30.74s, where the maximum difference is about 0.9W. Fig. 13(e) shows the T_2's average junction temperature T_{ave_a}, T_{ave_b} , T_{ave_c} in phase A, phase B and phase C are unbalanced before 30.74s, where the maximum difference is about 0.6℃. Since 30.74s, the proposed strategy is enabled. Here, the T_2's P_{ave_a}, P_{ave_b}, P_{ave_c} in phase A, phase B and phase C become balance and the T_2's T_{ave_a}, T_{ave_b} , T_{ave_c} in phase A, phase B and phase C becomes balance.

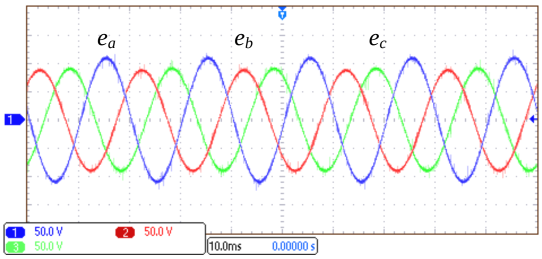

(a)

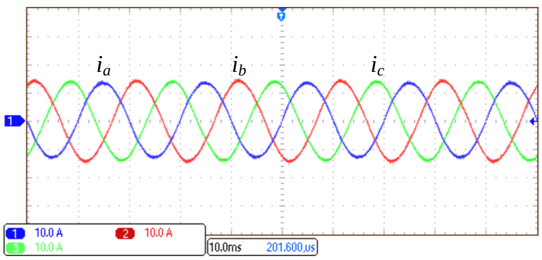

(b)

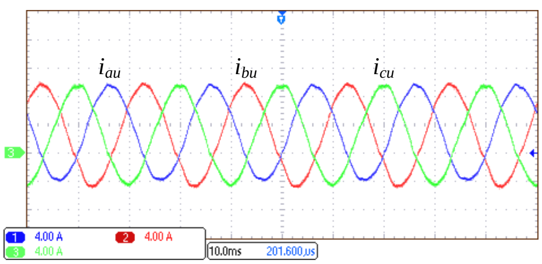

(c)

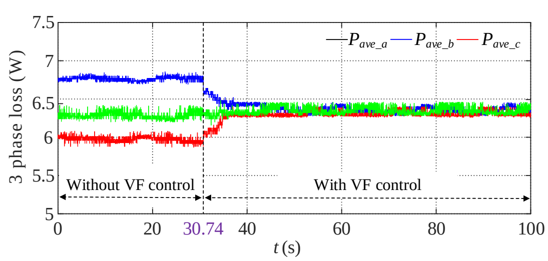

(d)

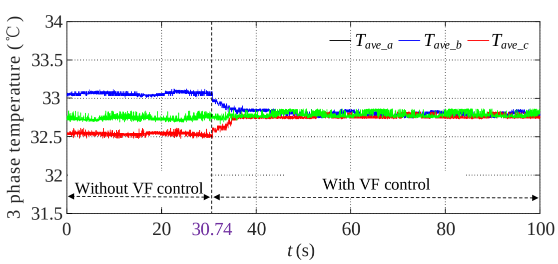

(e)

Fig. 13. (a) e_a, e_b and e_c. (b) i_a, i_b, and i_c. (c) i_{ua}, i_{ub}, and i_{uc}. (d) P_{ave_a}, P_{ave_b} and P_{ave_c}. (e) T_{ave_a}, T_{ave_b} and T_{ave_c}.

VII. CONCULUSION

In this paper, the SM temperature distribution among three phases of the MMC under unbalanced grid voltages is analyzed in details. The unbalanced grid voltages result in the unbalanced arm current among three phases, and leads to unbalanced SM power losses distribution among three phases, and therefore causes the temperature unbalance among three phases of the MMC. A VF strategy is proposed to improve the reliability of the MMC under unbalanced grid voltages. Through the regulation of the carrier frequency in each phase, the power loss among three phases can be kept balanced, and therefore the temperature distribution among three phases can be kept balanced, which can improve the reliability of the MMC under unbalanced grid voltages. The simulation and experiment results show the effectiveness of the proposed strategy.

REFERENCES

[1] Q. Yu, F. Deng, C. Liu, J. Zhao, F. Blaabjerg and S. Abulanwar, "DC-Link High-Frequency Current Ripple Elimination Strategy for MMCs Using Phase-Shifted Double-Group Multicarrier-Based Phase-Disposition PWM," *IEEE Trans. Power Electron.*, vol. 36, no. 8, pp. 8872-8886, Aug. 2021.

[2] F. Deng et al., "Protection Scheme for Modular Multilevel Converters Under Diode Open-Circuit Faults," *IEEE Trans. Power Electron.*, vol. 33, no. 4, pp. 2866-2877, April. 2018.

[3] Y. Zhang, H. Wang, Z. Wang, F. Blaabjerg and M. Saeedifard, "Mission Profile-Based System-Level Reliability Prediction Method for Modular Multilevel Converters," *IEEE Trans. Power Electron.*, vol. 35, no. 7, pp. 6916-6930, July. 2020.

[4] J. Lyu, X. Zhang, X. Cai and M. Molinas, "Harmonic State-Space Based Small-Signal Impedance Modeling of a Modular Multilevel Converter With Consideration of Internal Harmonic Dynamics," *IEEE Trans. Power Electron.*, vol. 34, no. 3, pp. 2134-2148, March. 2019.

[5] C. Liu, F. Deng, Q. Heng, X. Cai, R. Zhu and M. Liserre, "Crossing Thyristor Branches-Based Hybrid Modular Multilevel Converters for DC Line Faults," *IEEE Trans. Ind. Electron.*, vol. 68, no. 10, pp. 9719-9730, Oct. 2021.

[6] "Power quality-Three-phase voltage unbalance," GB/T 15543-2008.

[7] F. Deng et al., "Power Losses Control for Modular Multilevel Converters Under Capacitor Deterioration," *IEEE J. Emerg. Sel. Topics Power Electron.*, vol. 8, no. 4, pp. 4318-4332, Dec. 2020.

[8] M. Andresen, K. Ma, G. Buticchi, J. Falck, F. Blaabjerg and M. Liserre, "Junction Temperature Control for More Reliable Power Electronics," *IEEE Trans. Power Electron.*, vol. 33, no. 1, pp. 765-776, Jan. 2018.

[9] W. Li *et al*., "Thermal Optimization of Modular Multilevel Converters With Surplus Submodule Active-Bypass Plus Neutral-Point-Shift Scheme Under Unbalanced Grid Conditions," *IEEE J. Emerg. Sel. Topics Power Electron.*, vol. 7, no. 3, pp. 1777-1788, Sept. 2019.

[10] J. Sheng et al., "Active Thermal Control for Hybrid Modular Multilevel Converter Under Overmodulation Operation," *IEEE Trans. Power Electron*., vol. 35, no. 4, pp. 4242-4255, April. 2020.

[11] J. Sheng et al., "Active Thermal Control of Hybrid MMC Under Over-Modulation Operation," in *Proc. PEAC* 2018, pp. 1-6.

[12] J. Gonçalves, D. J. Rogers, J. Liang, "Submodule temperature regulation and balancing in modular multilevel converters", *IEEE Trans. Ind. Electron.*, vol. 65, no. 9, pp. 7085-7094, Jan. 2018.

[13] F. Hahn, M. Andresen, G. Buticchi and M. Liserre, "Thermal Analysis and Balancing for Modular Multilevel Converters in HVDC Applications," *IEEE Trans. Power Electron.*, vol. 33, no. 3, pp. 1985-1996, March. 2018.

[14] F. Hahn, G. Buticchi and M. Liserre, "Active thermal balancing for modular multilevel converters in HVDC applications," in *Proc. EPE'16 ECCE Europe* 2016, pp. 1-10.

[15] D. Wang, J. Liu, R. Cao, Y. Zhang, S. Song and X. Chen, "An Improved Active Thermal Balancing Algorithm for Modular Multilevel Converter in HVDC Applications," in *Proc. APEC* 2020, pp. 351-357.

[16] M. K. Bakhshizadeh, K. Ma, P. C. Loh and F. Blaabjerg, "Indirect thermal control for improved reliability of Modular Multilevel Converter by utilizing circulating current," in *Proc. APEC* 2015, pp. 2167-2173.

[17] G. A. Reddy and A. Shukla, "Circulating Current Optimization Control of MMC," *IEEE Trans. Ind. Electron*, vol. 68, no. 4, pp. 2798-2811, April. 2021.

[18] J. Zhao, F. Deng, W. Hu, Y. Du and S. Abulanwar, "Thermal Optimization Strategy Based on Second-Order Harmonic Circulating Current Injection for MMCs," *IEEE Access*, vol. 9, pp. 80183-80196, 2021.

[19] F. Deng, C. Liu, Q. Wang, R. Zhu, X. Cai and Z. Chen, "A Currentless Submodule Individual Voltage Balancing Control for Modular Multilevel Converters," *IEEE Trans. Ind. Electron.*, vol. 67, no. 11, pp. 9370-9382, Nov. 2020.

[20] M. Hagiwara and H. Akagi, "Control and Experiment of Pulsewidth-Modulated Modular Multilevel Converters," *IEEE Trans. Power Electron.*, vol. 24, no. 7, pp. 1737-1746, July. 2009.

[21] Weiqing Tao, Zhixia Gu, Leqin Wang and Jiaxi Li, "Research on control strategy of grid-connected inverter under unbalanced voltage conditions," in *Proc. IPEMC-ECCE Asia* 2016, pp. 915-919.

[22] Q. Tu, Z. Xu, and L. Xu, "Reduced switching-frequency modulation and circulating current suppression for MMCs," *IEEE Trans. Power Del*., vol. 26, no. 3, pp. 2009–2017, Jul. 2011.

[23] Y. Zhang, H. Wang, Z. Wang, Y. Yang and F. Blaabjerg, "Simplified Thermal Modeling for IGBT Modules With Periodic Power Loss Profiles in Modular Multilevel Converters," *IEEE Trans. Ind. Electron*., vol. 66, no. 3, pp. 2323-2332, March. 2019.

[24] Y. Dong, H. Yang, W. Li and X. He, "Neutral-Point-Shift-Based Active Thermal Control for a Modular Multilevel Converter Under a Single-Phase-to-Ground Fault," *IEEE Trans. Ind. Electron*., vol. 66, no. 3, pp. 2474-2484, March. 2019.

[25] D. Zhou, F. Blaabjerg, T. Franke, M. Tønnes and M. Lau, "Comparison of Wind Power Converter Reliability With Low-Speed and Medium-Speed Permanent-Magnet Synchronous Generators," *IEEE Trans. Ind. Electron*., vol. 62, no. 10, pp. 6575-6584, Oct. 2015.

[26] H. Qiu, J. Wang, P. Tu and Y. Tang, "Device-Level Loss Balancing Control for Modular Multilevel Converters," *IEEE Trans. Power Electron.*, vol. 36, no. 4, pp. 4778-4790, April. 2021.

[27] B. Wang *et al*., "Thermal Performances and Annual Damages Comparison of MMC Using Reverse Conducting IGBT and Conventional IGBT Module," *IEEE Trans. Power Electron.*, vol. 36, no. 9, pp. 9806-9825, Sept. 2021.